



Microstructural development and corrosion behavior of 13Cr–4Ni–1Mo martensitic stainless steel clad

A. Farzadi¹ · R. Kalantarian²

Received: 14 May 2020 / Accepted: 13 July 2020 / Published online: 22 July 2020
© International Institute of Welding 2020

Abstract

Martensitic stainless steels are deposited during manufacturing or repair to prolong the service life of a workpiece in a wide variety of industries such as steelmaking. The post-weld heat treatment (PWHT) is necessary to provide appropriate mechanical properties. In this research, a four-layer clad including a buffer and three layers of 13Cr–4Ni–1Mo stainless steel was deposited on AISI 4140 low-alloy steel using submerged arc welding. The effect of the PWHT on microstructure, corrosion behavior, and hardness of the layers was investigated. The double-loop electrochemical potentiokinetic reactivation (DL-EPR) was used to study the degree of sensitization (DOS). The microstructure in the as-welded condition consists of martensite, 19% delta-ferrite, retained austenite and carbide precipitates. The hardness value of the top layer in the as-welded condition is 469 ± 8 HV. The precipitates are bond to the delta-ferrite as a preferred nucleation site at 540 °C. The preferred nucleation site for precipitation and the DOS varies with changing in the PWHT temperature. The PWHT results in the formation of tempered martensite, a decrease in the hardness, and an increase in the DOS.

Keywords Post-weld heat treatment (PWHT) · DL-EPR · Degree of sensitization · Overlay · Delta-ferrite · Continuous casting roll

1 Introduction

Martensitic stainless steels containing 13 wt.% Cr extensively use in the manufacture of components with good tensile strength, wear resistance, and creep and fatigue strength, as well as moderate corrosion resistance and heat resistance up to approximately 650 °C. These alloys can be used in a wide range of applications such as compressor blades, continuous casting rolls, and cutting tools [1–3].

In order to provide moderate corrosion resistance and a right combination of mechanical properties, a heat treatment process involving heating followed by quenching is applied to this type of stainless steel. Subsequent tempering is essential to improve

toughness. A weld clad is a relatively thick layer of metal deposited on metal components to improve the corrosion resistance or to repair. The cladding is an effective and low-cost technique to extend service life.

The prevention of failure in harsh service environments of the continuous casting rolls requires to have excellent mechanical, corrosion, and wear properties. Hence, the continuous casting rolls are repaired by deposition of martensitic stainless steels containing 13 wt.% Cr. Vinas et al. [3] analyzed the failure of the continuous casting rolls to identify the origin of the cracks. They proposed that the contribution of Cr carbides to the tribo-degradation processes of the renovated surface layers be essential. Toit and Van Niekerk [4] examined the effects of the PWHT on microstructure and mechanical properties of a martensitic stainless steel, which is used for cladding the continuous casting rolls. A temperature below 500 °C was suggested to prevent softening and carbide precipitation.

Some researchers have studied the effects of heat treatment on the properties of 13Cr stainless steels. Zhang et al. [5] investigated the microstructure and amount of retained austenite in 13Cr–4Ni ($C = 0.05$ wt.%) martensitic stainless steel during intercritical tempering at 620 °C. They found that the amount of retained austenite increases initially, reaches a maximum, and then decreases, as the intercritical tempering holding time increases. Some reversed austenite may transform

Recommended for publication by Commission II - Arc Welding and Filler Metals

✉ A. Farzadi
farzadi@aut.ac.ir

¹ Department of Materials and Metallurgical Engineering, Amirkabir University of Technology (Polytechnic of Tehran), Hafez Ave., Tehran 15916-34311, Iran

² Central Workshop, Khuzestan Steel Company (KSC), Ahvaz, Iran

Table 1 Chemical composition (wt.%) and estimated transformation temperatures of base metal, and the layers of the overlay

Element	C	Si	Mn	P	S	Cr	Ni	Mo	Al	Cu	Ti	Nb	V	M_S temperature (°C)	A_{C1} temperature (°C)
Base metal	0.38	0.26	1.25	0.024	0.022	0.85	0.03	0.20	0.03	0.02	0.010	0.002	0.002	-	-
First (buffer) layer	0.24	0.36	1.47	0.023	0.016	1.20	0.04	0.36	0.02	0.09	0.011	0.002	0.002	371	682
Second layer	0.15	0.52	1.20	0.022	0.010	8.14	2.26	0.76	-	0.05	0.012	0.002	0.060	253	477
Third layer	0.10	0.60	1.10	0.021	0.010	10.56	3.12	0.86	-	0.04	0.017	0.002	0.070	216	564
Forth (top) layer	0.09	0.67	1.015	0.022	0.008	12.81	3.89	0.97	-	0.03	0.008	0.002	0.004	163	589

back to martensite during the cooling process. J.-Y Park and Y.-S Park [2] investigated the effect of austenitizing temperature on properties of 14Cr-3Mo martensitic stainless steels containing 0.15 and 0.3 wt.% C. As C content rises owing to the dissolution of carbides, martensite start temperature (M_S) decreases. Silva et al. [6] investigated the influences of the tempering parameters on the microstructure, mechanical properties, and sensitization of a Ti-alloyed supermartensitic stainless steel ($C = 0.0278$ wt.%). The degree of sensitization (DOS) increases continuously by increasing the tempering temperature above 400 °C.

The microstructure and properties of the weld zone in 13Cr-4Ni stainless steels have also been examined in the literature. Mokhtabad et al. [7] studied the microstructure of single-pass and double-pass welds in low-carbon ($C = 0.022$ wt.%) 13Cr-4Ni martensitic steel. They observed that the microstructure of the weld metal contains columnar grains filled with fine martensite laths. Traces of dendritic delta-ferrite were found in the heat-affected zone (HAZ) close to the fusion line. Divya et al. [8] studied the role of delta-ferrite in weld metals containing a high amount of Cr and Ni under different post-weld heat treatment (PWHT) conditions. They reported that the microstructure of 14.5Cr-5Ni weld metal ($C = 0.05$ wt.%) consists of martensite, retained austenite, and delta-ferrite in the as-welded condition. The decreased M_S increases the amount of retained austenite. Akselsen et al. [9] examined microstructure-property relationships in the HAZ of low-carbon ($C = 0.01$ – 0.11 wt.%), 13% Cr martensitic stainless steels. They reported hardness values beyond 300 kgf/mm² for the steels with 0.11 wt.% C. The Schaeffler diagram should be used with care for the steels with 0.028 wt.% C. Thibault et al. [10] characterized the

microstructure and obtained the distribution of residual stresses in the HAZ of low-carbon ($C = 0.02$ wt.%) 13Cr-4Ni martensitic steel. They proved that PWHT lowers the cracking susceptibility due to the decreased residual tension and tempered martensite. Bilmes et al. [11] studied the effect of PWHT on microstructures and mechanical properties of 13Cr-4Ni soft martensitic stainless steel welds containing Mo ($C = 0.06$ wt.%). They found that the presence of tempered martensite and austenite in microstructure increases ductility, and the presence of delta-ferrite decreases it. Microstructural development and properties strongly depend on the C content, Cr content, and heat treatment.

The above literature survey indicates that the use of PWHT is an obvious method to improve the mechanical properties. However, such a heat treatment can have a deleterious effect on corrosion resistance. The simultaneous effects of the PWHT on the microstructure and corrosion behavior, particularly the DOS, of stainless steel clads have not received much attention in the literature. Therefore, a four-layer clad, which is composed of a buffer layer and three surfacing layers, was deposited on a low-alloy steel using submerged arc welding (SAW) process. The SAW process was used due to the high deposition rate. The top (fourth) layer of the clad is 13Cr-4Ni-1Mo stainless steel. Transformation temperatures are the critical factors in determining the PWHT conditions.

2 Materials and methods

AISI 4140 (DIN EN 42CrMo4) low-alloy steel plates with the dimensions of 450 mm × 250 mm × 25 mm were used. A four-layer clad was deposited onto the surface of the plates using

Table 2 Welding parameters for buffer layer and three other layers

Parameter	Wire diameter (mm)	Current (A)	Voltage (V)	Welding speed (cm/min)	Contact tube to work distance (mm)
Buffer layer	2.4	350	30	30	30
Three other layers	3.2	350	34	30	30

Table 3 PWHT conditions and measured hardness values of each layer of overlay in as-welded condition and after PWHT

Sample	Temperature (°C)	Time (h)	Hardness value (HV)			
			First (buffer) layer	Second layer	Third layer	Fourth layer
As-welded	-	-	328 ± 20	508 ± 20	470 ± 18	469 ± 4
P1	420	2	331 ± 17	393 ± 4	441 ± 17	465 ± 8
P2	500	2	322 ± 15	390 ± 14	484 ± 7	452 ± 8
P3	540	2	284 ± 8	390 ± 7	369 ± 8	360 ± 4
P4	580	2	318 ± 7	391 ± 8	376 ± 14	340 ± 19
P5	580	8	336 ± 6	356 ± 3	340 ± 13	350 ± 13

SAW. The compositions of the as-received plate and the four deposited layers were measured and given in Table 1. Optical emission spectroscopy (OES) was used to determine the chemical composition of the plate and the deposited layers. At least three measurements for each composition was carried out. The chemical analysis is conducted after the material has been removed from the surface (2 mm under the surface).

Although SAW is a high deposition rate process, dilution in this process is high. Hence, the four-layer clad was deposited to reach the chemical composition of the filler metal. A low-carbon buffer layer was first deposited with a DIN 8555 UP1-GF-250-P flux-cored wire. The workpiece was then surfaced with three layers of a DIN 8555 UP-9-GF-40-CG flux-cored wire that produces a corrosion-resistant deposit with the composition of 13Cr-4Ni-1Mo. Flux-cored wires have the benefit of being easily formulated for a particular application. The submerged arc welds were made using a direct constant (DC) power supply (maximum 1200 A). The welding wire was positively polarized, and the workpiece was negative. The welding flux was EN 760 S A FB 1 55 AC H5 (AWS 5.17 F7A2-EM12). The welding conditions were adopted from the literature [12, 13] to achieve a desired weld bead shape (shallow and wide) and a higher deposition rate. The welding condition for the buffer layer and the three other layers was given in Table 2. The preheat temperature and the maximum inter-pass temperature were 225 °C and 350 °C, respectively. The resulting weldment was 200 mm wide and 300 mm long. After welding, the clad workpiece was subjected to penetrant testing (PT) and found to be defect-free on the surface. In order to examine the effect of PWHT on

the microstructure and the hardness of the weld deposits, several 10 mm × 10 mm samples were machined of the clad workpiece. These samples were exposed to five PWHTs, which are listed in Table 3. The PWHT temperature range was determined according to the calculation of lower-critical temperature (A_{C1}) for the top layer of the clad (Table 1) and the literature [7, 9, 10]. For heat treatment, an electric muffle furnace was used. The furnace was heated up to the PWHT temperature. Then, the sample was fed into the furnace. After holding for the PWHT duration, they cooled in air. A CHY 806A thermometer and a K-type thermocouple were used to control the furnace temperature in the holding time.

For metallographic examinations, the samples were sectioned, ground up to 2000 grit SiC paper, and polished with 0.3 μm alumina. In order to identify any microstructural constituents, the specimens were chemically or electrochemically etched in several etching solutions.

In order to reveal a particular phase in the microstructure, several etching reagents were used. The polished specimens were etched in Vilella's reagent and chromic acid solution to reveal the overall microstructure [8, 14]. Also, the specimens were electrochemically etched in an oxalic acid solution and in sodium hydroxide solution to reveal the carbide precipitates and delta-ferrite, respectively [11, 15–18]. The Etchants used in this study and their composition, and etching condition are given in Table 4. All etching processes were done at room temperature. An Olympus BH2 optical microscope (OM) and a Tescan Vega II scanning electron microscope (SEM) were used for microstructure observations. In order to determine the volume fraction of delta-ferrite, the optical

Table 4 Etchants used in this study and their composition, etching condition

Etchant	Composition	Etching condition	Comment
Vilella's reagent	1 g picric acid, 5 mL HCl, 100 mL ethanol	50–70 s	Reveals overall microstructure
Chromic acid solution	2 g CrO ₃ , 100 mL H ₂ O	Electrochemical etch at 6 V, 20 s	Reveals overall microstructure
Oxalic acid solution	C ₂ H ₂ O ₄ 10 g, 100 mL H ₂ O	Electrochemical etch at 5–6 V, 20 s	Reveals carbide precipitates
Sodium hydroxide solution	20 g NaOH, 100 mL H ₂ O	Electrochemical etch at 6 V, 6 s	Outlines delta-ferrite

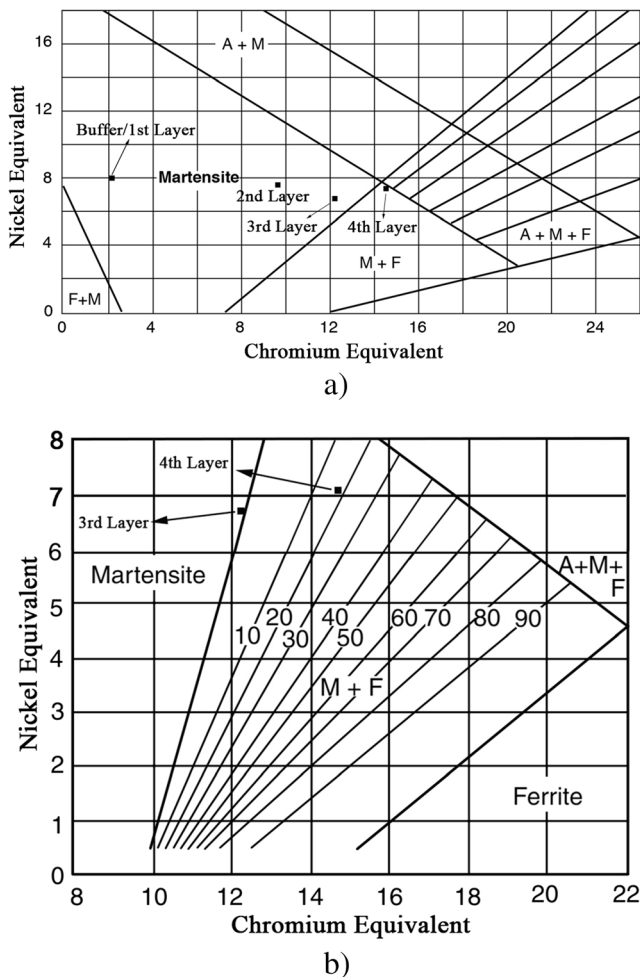


Fig. 1 Prediction of the microstructure in layers using **a** Schaeffler [25] and **b** Balmforth [20] diagrams

micrographs, which had been etched by NaOH solution, were processed using the ImageJ 1.44 software at the magnification of $\times 100$. A series of images were taken from the specimen. The intensity threshold method was employed to highlight regions of delta-ferrite. The ratio of the whole area of these regions to the total area was considered the volume fraction [19]. X-ray diffraction (XRD) was carried out using Philips XPert MPD X-ray diffractometer with Co- K_{α} radiation in as-welded and post-weld heat-treated samples to analyze retained austenite. The XRD profiles were recorded in the 2θ angular range of 20 to 105° with the step size of 0.02° . Vickers hardness tests were carried out using a load of 10 kgf. Each hardness value represents the average of at least three measurements.

$$M_S(^{\circ}\text{C}) = 562 - (354C + 29.7\text{Mn} + 31.7\text{Ni} + 12.5\text{Cr} + 17.4\text{Ni} + 20.8\text{Mo}) - 13.4(\text{Ni} + \text{Cr}) + 22.4(\text{Cr} + \text{Mo}) \times C \quad (7)$$

Equation (8) was proposed by TWI [23] to estimate the A_{C1} for 13 wt.% Cr steels with less than 0.05 wt.% C.

The double-loop electrochemical potentiokinetic reactivation (DL-EPR) test was carried out to calculate the DOS. Before electrochemical experiments, the specimens were ground, and polished, similar to the method was performed for the metallographic specimens. The solution was composed of 0.5 M sulfuric acid (H_2SO_4) and 0.01 M potassium thiocyanate (KSCN) in the distilled water. The saturated calomel electrode (SCE) was used as the reference electrode. The potential was swept from 50 mV below the open circuit potential to +800 mV vs SCE at the rate of 1.67 mV/s. The DOS can be calculated by Eq. 1 [1].

$$\text{DOS} = \frac{Q_r}{Q_a} \times 100 \quad (1)$$

where Q_r and Q_a are the areas under (the electric charge involved in) the reactivation and activation parts of the current-time curve, respectively. The electrochemical experiments were done at least four times for each sample to obtain the repeatability.

The Schaeffler and Balmforth diagrams are used to predict the microstructure in the overlay. The chromium and nickel equivalent values (Cr_{eq} and Ni_{eq}) for Schaeffler diagrams are calculated from Eqs. (2) and (3), respectively [8].

Schaeffler formulas:

$$\text{Cr}_{\text{eq}} = \text{Cr} + \text{Mo} + 1.5 \times \text{Si} + 0.5 \times \text{Nb} \quad (2)$$

$$\text{Ni}_{\text{eq}} = \text{Ni} + 30 \times \text{C} + 0.5 \times \text{Mn} \quad (3)$$

In order to determine the microstructure accurately and the ferrite content, Balmforth diagram can be used. The chromium and nickel equivalent values (Cr_{eq} and Ni_{eq}) are calculated from Eqs. (4) and (5), respectively [20].

Balmforth formulas:

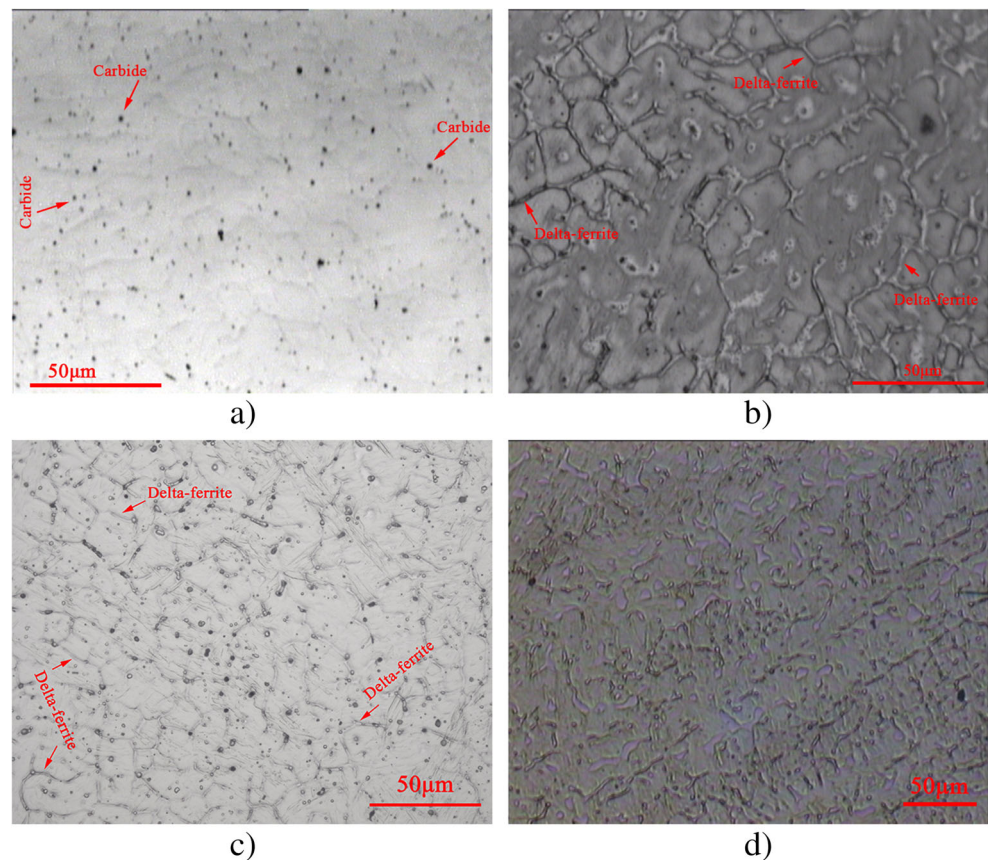
$$\text{Cr}_{\text{eq}} = \text{Cr} + 2 \times \text{Mo} + 10 \times (\text{Al} + \text{Ti}) \quad (4)$$

$$\text{Ni}_{\text{eq}} = \text{Ni} + 35 \times \text{C} + 20 \times \text{N} \quad (5)$$

The temperature range over which the martensite forms is mainly dependent on composition. All alloying elements, except cobalt, tend to decrease the M_S . In order to estimate the M_S , Eqs. (6) and (7) were proposed by Gooch [21] for stainless steels and Self [22] for low-alloy steels, respectively.

$$M_S(^{\circ}\text{C}) = 540 - (497C + 6.3\text{Mn} + 36.3\text{Ni} + 10.8\text{Cr} + 46.6\text{Mo}) \quad (6)$$

Fig. 2 Optical microstructure of top layer of overlay in the as-welded condition. Etched by **a** oxalic acid, **b** NaOH, **c** chromic acid, and **d** Vilella's reagent



$$A_{C1}(\text{°C}) = 850 - 1500(C + N) - 50\text{Ni} - 25\text{Mn} + 25\text{Si} + 25\text{Mo} + 20(\text{Cr} - 10) \quad (8)$$

Equation (9) was also proposed for low-alloy steels [24].

$$A_{C1}(\text{°C}) = 723 - 20.7\text{Mn} - 16.9\text{Ni} + 29.1\text{Si} - 16.9\text{Cr} \quad (9)$$

3 Results and discussion

3.1 Prediction of microstructure

Based on the chemical composition given in Table 1, the microstructure in layers of the overlay is predicted in Fig. 1. The predicted microstructure in each layer of the overlay is illustrated in Fig. 1a. The predicted microstructure in the first (buffer), second, and third layers is fully martensitic, but the fourth layer consists of martensite and ferrite. Also, the predicted microstructure in the third and fourth layers of the overlay is illustrated in Fig. 1b. The similar microstructures are predicted by the Schaeffler [25] and Balmforth [20] diagrams in each layer, as shown in Fig. 1 a and b. The predicted microstructure in the first (buffer), second, and third layers is fully martensitic. Also, the predicted microstructure in the

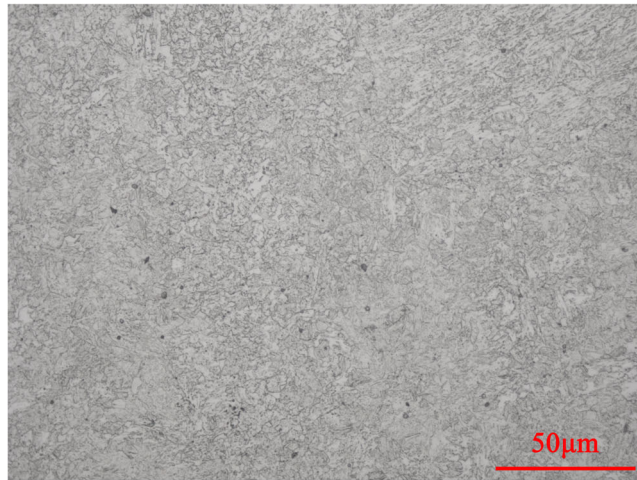
fourth layer includes martensite and ferrite. The predicted ferrite content in the fourth layer is about 17%. The difference between the predicted and measured ferrite contents can arise from the accuracy of the chemical analysis used in this research. High-temperature combustion method is more accurate than OES in measuring carbon.

3.2 Transformation temperature

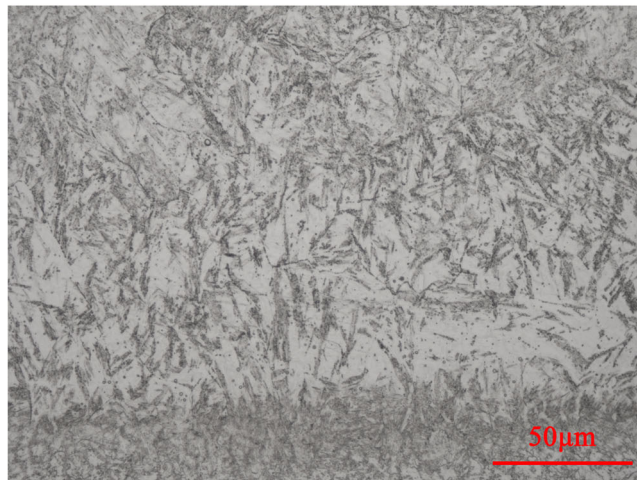
The calculated transformation temperatures (M_S and A_{C1}) of all layers are given in Table 1. The M_S and A_{C1} temperatures of the first (buffer) layer are calculated by Eqs. (7) and (9), respectively. For the three other layers, 13Cr-4Ni-1Mo stainless steel layers, Eqs. (6) and (8), are used. Equations (6) to (9) are successful at predicting the transformation temperature in a given range of composition [21–24].

In most martensitic stainless steels, the M_S temperature is in the range of 200 to 400 °C [24]. The transformation to martensite is completed at room temperature for these steels because the martensite finish temperature (M_F) is at least 100 K below the M_S [24]. In the fourth layer of the overlay, the M_S temperature is 163 °C, and the M_F temperature may be below room temperature. Hence, some austenite can be retained in the microstructure. As given in Table 1, the A_{C1} temperature for the second layer is 477 °C and for the fourth layer is 589 °C. The low A_{C1} temperature can pose a problem during

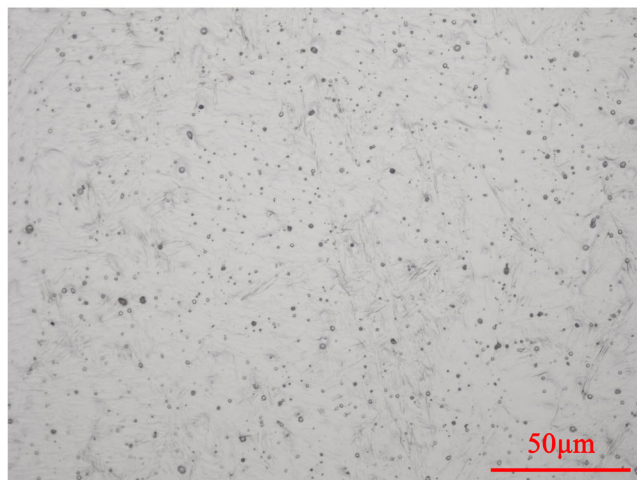
PWHT because temperatures above 600 °C are usually used to temper martensitic steels. Below 600 °C, the diffusion rate



a)



b)



c)

Fig. 3 Optical microstructure of **a** first (buffer), **b** second, and **c** third layers in the as-welded condition. Etched by Chromic acid reagent

is relatively low, and the tempering time may be very long [26]. Austenite forms during the tempering above A_{C1} . This austenite may have a subsequent loss in properties. Austenite can transform to fresh martensite upon cooling if it is retained to room temperature, or decomposes into ferrite and pearlite during PWHT [19]. Diffusion rate and solubility of elements in austenite are entirely different.

3.3 Composition and microstructure

The chemical composition of each layer of the overlay is given in Table 1. The amount of the alloy elements, except C, in the first (buffer) layer is comparable with that in the base metal. The amount of C in this layer is much lower than that in the base metal. This is the reason why it is called “buffer.” The buffer layer has two essential tasks: (1) balancing of strong chemical gradients between the base and clad materials, and (2) improvement of clad quality in terms of cracking and adhesive strength of hard facing clads. In the next layers, the decrease in C and the increase in Cr, Ni, and Mo are observed.

In Fig. 2, the microstructure of the top layer (fourth layer) in the as-welded condition is shown. The carbide precipitates were revealed by oxalic acid solution (Fig. 2a). The distribution and the size of the carbides are distinct. Some isolated carbide particles and no continuous film of carbide are observed. The NaOH solution outlined delta-ferrite effectively, as shown in Fig. 2b. This solution can be proper when image analyzing is necessary. The volume fraction of the delta ferrite is approximately 19%. The chromic acid solution attacked carbides and outlined delta-ferrite slightly (Fig. 2c). In comparison with Fig. 2b, the ferrite interfaces are barely distinguishable. Vilella’s reagent etches martensite somewhat and outlined carbides and delta-ferrite, as shown in Fig. 2d. The primary microstructural constitutions have been visible in Fig. 2 c and d. None of the solutions had been successful in etching (attacking) fresh martensite clearly.

Overall, the microstructural examination of the UP-9-GF-40-CG deposit in the as-welded condition reveals a martensitic microstructure with some delta-ferrite located at the boundaries of the primary dendrites and some carbide particles in the top layer. The optical micrographs of the microstructure in the first (buffer), second, and third layers of the clad in the as-welded condition are shown in Fig. 3. The microstructure in these three layers consists of the martensite; however, the martensite morphology is different due to the difference in the composition. By comparison of the microstructural examinations in the four layers of the clad with the predicted microstructure in section 3.1, it can be concluded that the Schaeffler and the Balmforth diagrams can predict microstructure and the Balmforth diagram can estimate the ferrite content, in 13Cr-4Ni-1Mo stainless steel clad.

Based on the calculated phase diagram for a 12 %Cr martensitic stainless steel [25], it seems that the transformation sequence is as follow:

Liquid \rightarrow Liquid + Primary ferrite + (Austenite + Eutectic ferrite) \rightarrow Primary ferrite + Austenite + Eutectic ferrite \rightarrow Austenite + Eutectic ferrite \rightarrow Martensite + Eutectic ferrite.

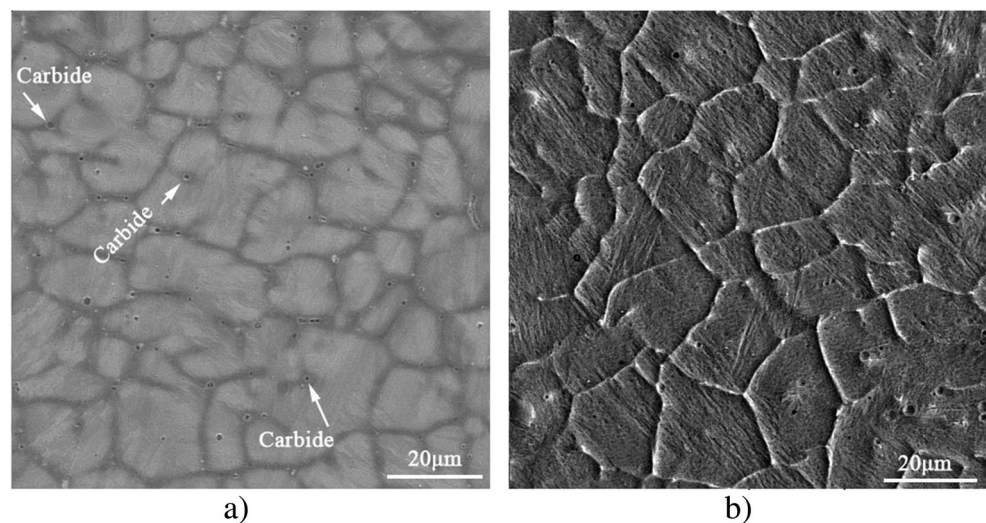
The segregation of C and other alloying elements during solidification can result in the formation of a mixture of ferrite and austenite between the dendrite arms during the terminal stage of solidification. This ferrite is called the eutectic ferrite [24, 25]. It may be sufficiently enriched in ferrite-promoting elements, particularly Cr and Mo. Hence, it does not transform to austenite on cooling below the solidification temperature range. However, the primary ferrite at the dendrite cores transforms to austenite through the post-solidification phase transformation. Upon cooling, the austenite transforms to martensite below M_s . The eutectic ferrite resides along the solidification grain and sub-grain boundaries, and the final weld microstructure consists of a mixture of martensite and eutectic ferrite [25]. Besides, some carbide precipitation occurs on cooling. The carbide particles are isolated. Also, continuous films of grain boundary carbide are not observed (Fig. 2a). Thus, this microstructure can be susceptible to intergranular corrosion, which is caused by sensitization or precipitation of Cr carbide preferentially along grain boundaries during welding. Cr and C atoms rapidly diffuse from the adjacent matrix to the boundaries, where they combine to form Cr carbide. This precipitation produces a Cr-depleted region surrounding the boundaries. This region becomes anodic to the rest of the grain and hence is preferentially attacked in corrosive media, resulting in intergranular corrosion. The precipitation reduces the local corrosion resistance of the microstructure and promotes rapid attack of the grain boundary region.

In Fig. 4, the SEM micrographs of the microstructure in the as-welded sample are shown. Both NaOH and chromic acid

solutions are used to etch the as-welded sample. In the micrograph etched by NaOH solution (Fig. 4a), the darker etching features along the solidification sub-grains are delta-ferrite, and the darker etching points are carbides [23, 24]. The carbides are at the solidification sub-grains and into the dendrites. In the micrograph etched by chromic acid solution (Fig. 4b), the brighter etching features along the solidification sub-grains are delta-ferrite and the darker etching points are carbides. The carbides into the dendrites are only visible. The later solution etched martensite laths, but they were not visible in the optical micrograph (Fig. 2c).

The microstructure of the top layer (fourth layer) after PWHT is shown in Figs. 5 and 6. Based on the metallographic examinations of the as-welded sample, Vilella's reagent and oxalic acid solution were used for the post-weld heat-treated samples. As shown in Figs. 5a and 6a, the microstructure after PWHT at 420 °C for 2 h (in the sample P1) consists of slightly tempered martensite, delta-ferrite, and carbide precipitates. The carbide precipitation appears on the delta-ferrite interfaces after PHWT at 500 °C for 2 h, as shown in Figs. 5b and 6b. A higher density of precipitates and larger precipitates are observed, and martensite is tempered more in the sample P2, in comparison with the sample P1. This trend is followed in the sample P3, as shown in Fig. 5c. The optical micrographs in Figs. 5d and 6c suggest that PWHT at 580 °C for 2 h and 8 h results in extensive carbide precipitation and tempered martensite in the sample P4. The carbides precipitate at the martensite lath boundaries in the entire martensitic matrix of the samples P4 and P5 extensively. As a result, the increase in the PWHT temperature causes changing the preferred site for precipitation. At 540 °C and below it, the carbides precipitate at the delta-ferrite interfaces, but at 580 °C, the carbides precipitate at the martensite lath boundaries. Similar behavior was observed in the literature [11].

Fig. 4 Scanning electron microscopy images of the as-welded sample etched by **a** NaOH, **b** chromic acid



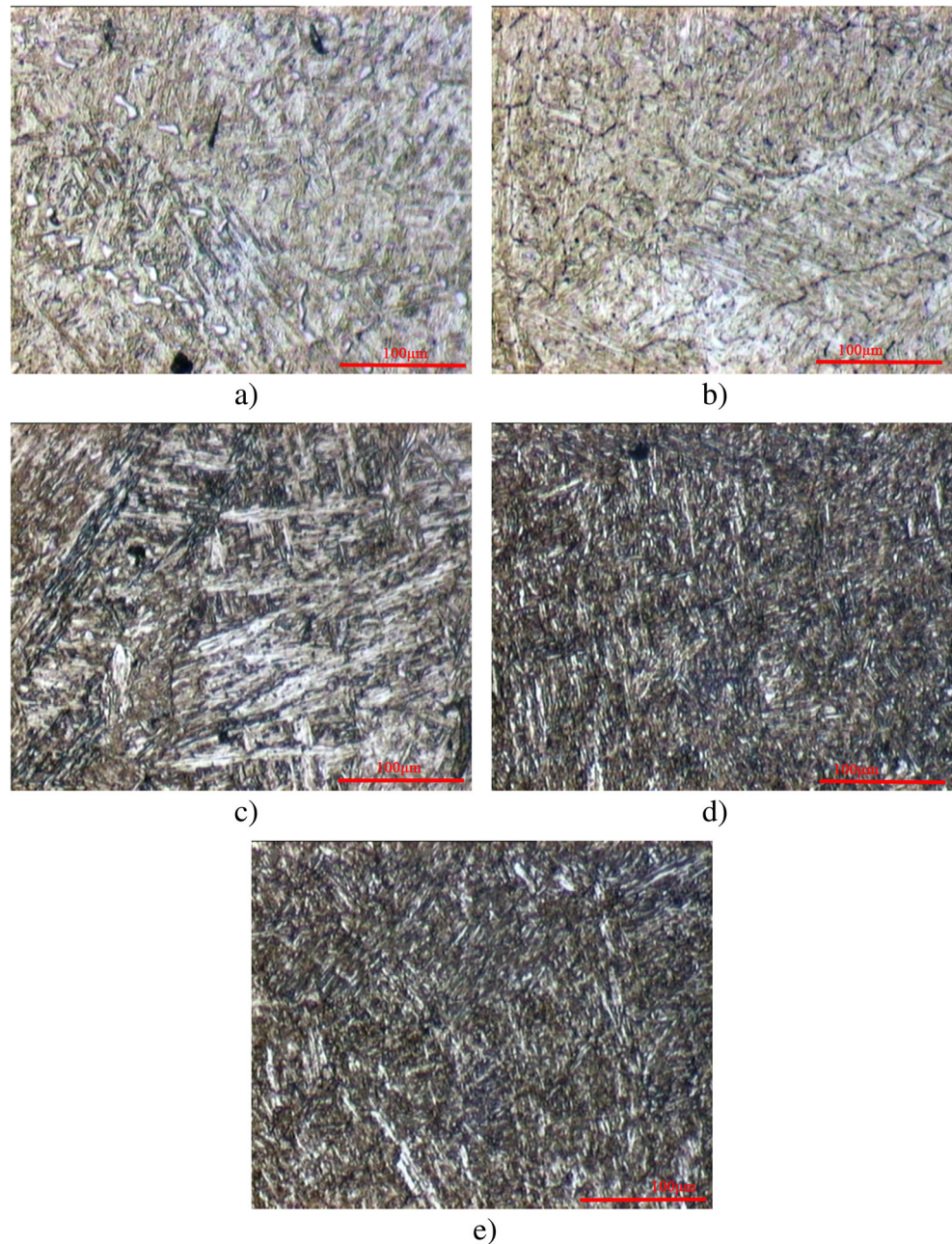
The XRD patterns of the as-welded and the post-weld heat-treated sample at 580 °C for 8 h (the samples P1 and P5) are shown in Fig. 7. The diffraction pattern of the as-welded sample presents the peaks of the ferrite and austenite phases. No retained austenite is evident in the OM micrographs (Fig. 2), due to the etching technique. However, the XRD measurements of the as-welded sample (Fig. 7a) reveal the retained austenite. It is probable that the retained austenite is in martensite-austenite constituents and embedded at the martensite lath boundaries. As given in Table 1, the M_S of the fourth layer is 163 °C. This low temperature may be the reason for the presence of the retained austenite in the microstructure [27].

The samples which are post-weld heat-treated at 500 and 580 °C, similar to the sample P5, show ferrite peaks only, and hence, the XRD patterns are not included in the article. Austenite can decompose into ferrite and pearlite during PWHT or transform to fresh martensite upon cooling to room temperature after PWHT.

3.4 Hardness

The hardness values of each layer of the overlay in the as-welded condition and after PWHT are given in Table 3. For the top (fourth) layer, PWHT at and above 500 °C for 2 h (the

Fig. 5 Optical microstructure of top layer of overlay after PWHT at **a** 420 °C for 2 h, **b** 500 °C for 2 h, **c** 540 °C for 2 h, **d** 580 °C for 2 h, and **e** 580 °C for 8 h. Etched by Vilella's reagent



samples P2-P5) decreases the hardness. The hardness value decreases from 467 to 452 HV (17 HV) after PWHT at 500 °C but tempering at 540 °C results in the considerable decrease of 109 HV (from 467 to 360 HV) in hardness. Extensive carbide precipitation is not observed after PWHT at 500 and 540 °C for 2 h (Fig. 6b). The hardness value decreases from 469 to 340 HV (129 HV) after PWHT at 580 °C for 2 h (the sample P4). The microstructure in the fourth layer of this sample consists of tempered martensite (Fig. 5d) and a substantial amount of Cr-rich $M_{23}C_6$ carbide (Fig. 6c). This microstructure can result in an increase in toughness [10], and susceptibility to intergranular corrosion [28]. The longer tempering time at 580 °C (8 h) has a little effect on hardness and microstructure. Therefore, the PWHT at 500 and 540 °C for 2 h is recommended depending on the required hardness on the surface. The hardness values of the first (buffer) layer are not affected by the PWHT. This may be because of the tempering effect of successive weld passes or upper layers.

3.5 Degree of sensitization

The results of the DL-EPR experiments for the as-welded sample and the post-weld heat-treated samples are shown in Fig. 8. By using the potentiodynamic polarization results and Eq. 1, the DOS is calculated and shown in Fig. 9. Indeed, the ratio of Q_r to Q_a indicates the fraction of the material depassivated due to Cr depletion [28]. The as-welded sample has the lowest DOS. Sensitization occurs in all post-weld heat-treated samples, even though at below 540 °C. Nonetheless, Taji et al. [1] reported that the highest DOS for 403 martensitic stainless steel occurs at the tempering temperature of 550 °C, and the sensitization did not observe at below 550 °C. The disagreement on the results can be explained by the presence of the considerable volume fraction of delta-ferrite in the microstructure.

The DOS for the sample P3 is lower than the other post-weld heat-treated samples. Therefore, the PWHT at 540 °C for 2 h is recommended to obtain more suitable mechanical and

Fig. 6 Scanning electron microscopy images of samples **a** P1, **b** P2, **c** P4, and **d** P5. Etched by oxalic acid

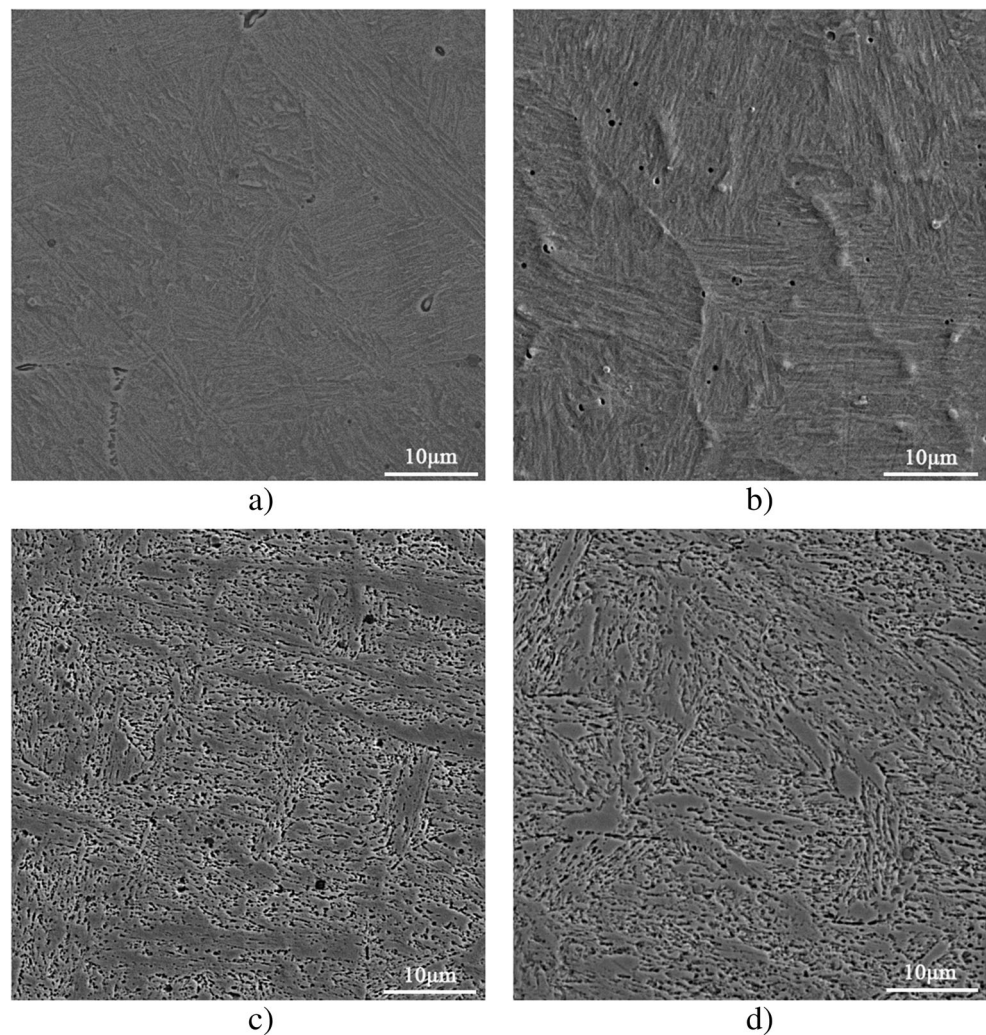
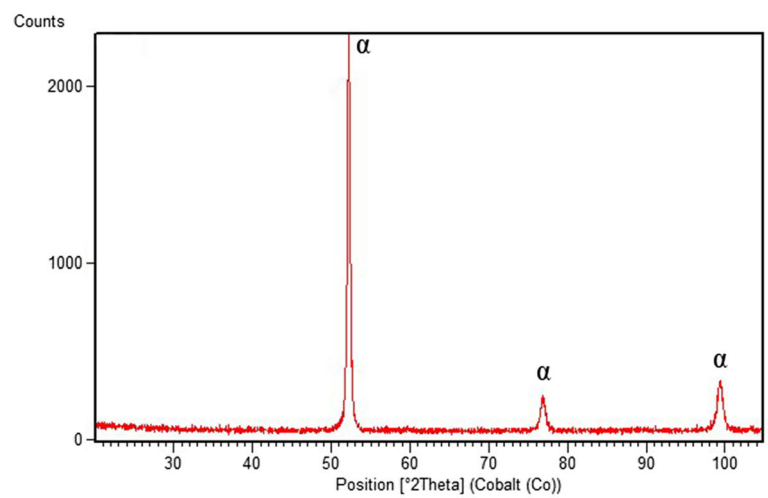
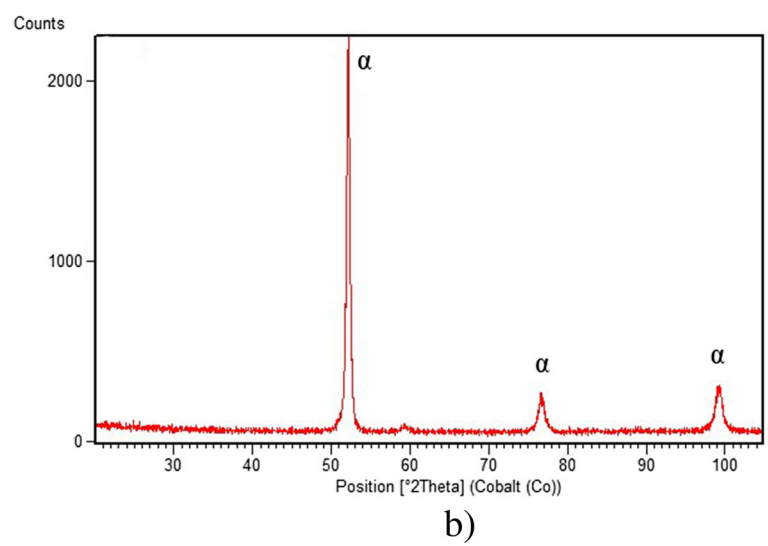
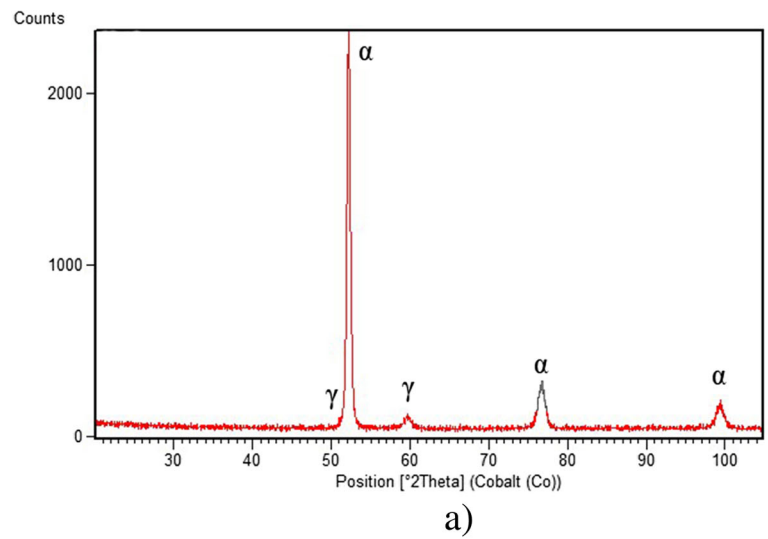


Fig. 7 XRD patterns of **a** as-welded sample, and samples **b** P1 and **c** P5



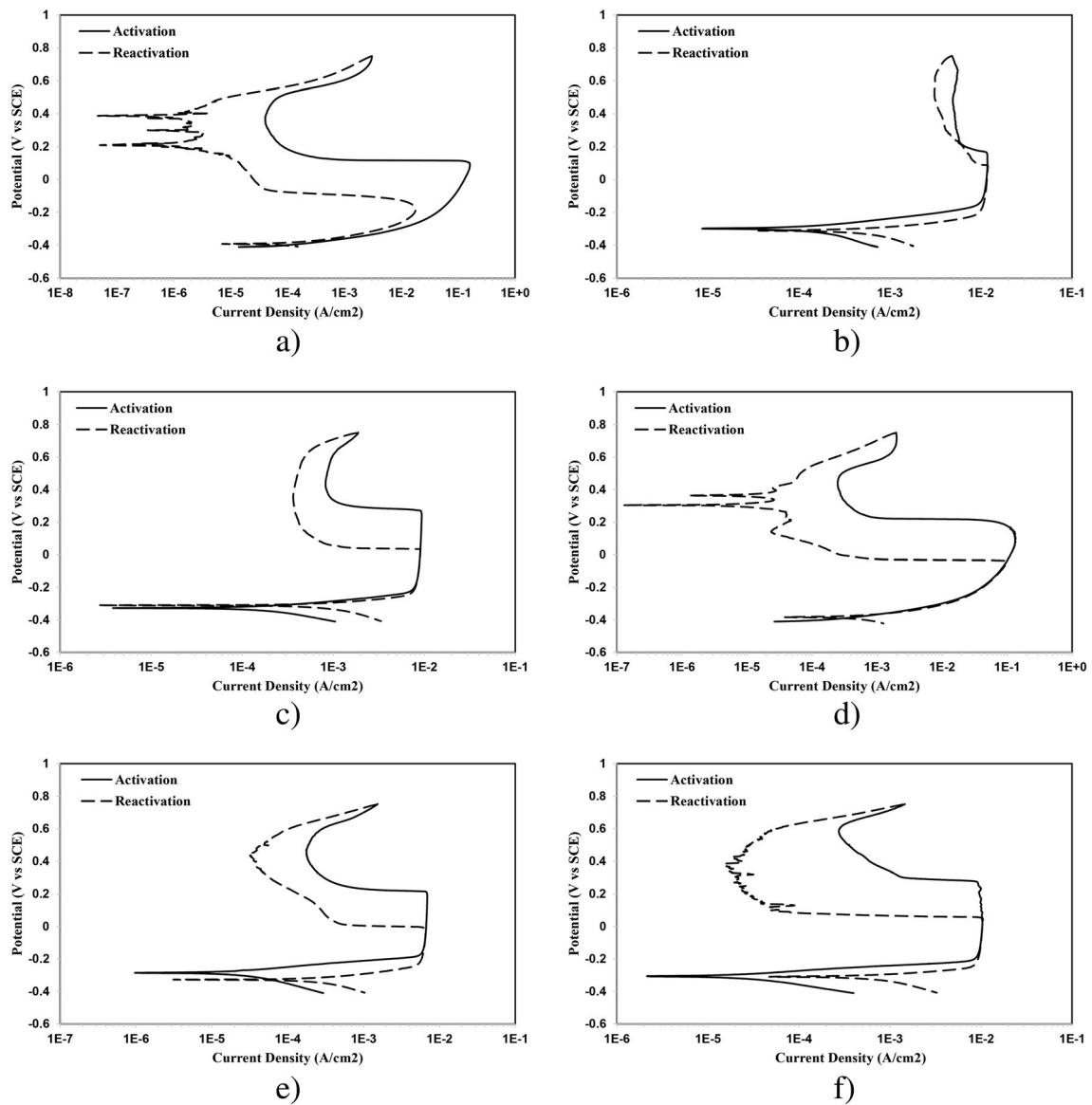
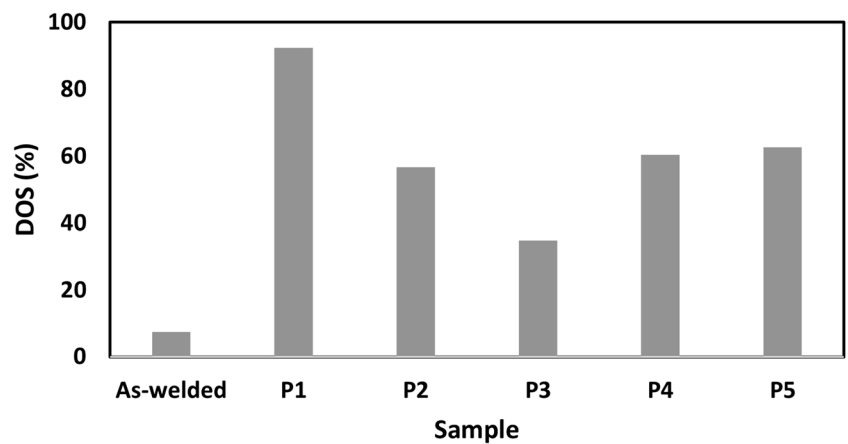


Fig. 8 Results of DL-EPR experiments of a as-welded sample, and samples b P1, c P2, d P3, e P4, and f P5

Fig. 9 Comparison between degree of sensitization (DOS) for as-welded sample and post-weld heat-treated samples



corrosion properties in the top layer. At 540 °C and below it, the microstructure is sensitized by decomposition of delta-ferrite into carbide. The PWHT at 580 °C for both 2 and 8 h increases the DOS, on account of the carbide precipitation at the martensite lath boundaries. As mentioned in section 3.3, the preferred site for precipitation of carbides is the delta-ferrite interfaces or martensite lath boundaries, depending on the temperature. Hence, it can be concluded that the DOS varies with changing in the precipitation behavior of carbides.

4 Conclusions

A four-layer clad, including a buffer layer and three surfacing layers, was deposited on AISI 4140 low-alloy steel using the SAW process. The top (fourth) layer of the overlay is 13Cr-4Ni-1Mo stainless steel with 0.09 wt.% C. The conclusions of the investigations are as follows:

1) In as-welded condition, the microstructure of the fourth layer consists of martensite, 19% delta-ferrite, retained austenite, and carbides. Both the Schaeffler and the Balmforth diagrams can be used to predict the microstructure, and the Balmforth diagram can be used to predict the ferrite content in 13Cr-4Ni-1Mo stainless steel clad. The hardness value is 469 ± 8 HV.

2) The carbides precipitate at the delta-ferrite interfaces by PWHT at 540 °C and below it, but the carbides precipitate at the martensite lath boundaries by PWHT at 580 °C. Thus, the preferred site for precipitation varies with changing in the PWHT temperature.

3) The PWHT in the temperature range of 420 to 580 °C leads to an increase in the degree of sensitization (DOS), compared with the as-welded condition. The DOS is affected by the transformation behavior of carbide precipitation.

4) The hardness values after PWHT at 540 °C decrease from 469 to 360 HV. Also, the DOS is the lowest in the post-weld heat-treated samples. Hence, PWHT at 540 °C for 2 h is recommended to obtain a more suitable mechanical and corrosion properties in the top layer.

Acknowledgments The authors are pleased to acknowledge assistance in performing the experiments from Mohammad Hossein Nooripoor and guidance of Kamran Taher, a senior engineer in the Research and Development Department of KSC.

Funding information This research was funded by the Khuzestan Steel Company (KSC) under Contract No. 52305572.

Compliance with ethical standards

Conflict of interest The authors declare that they have no conflict of interest.

References

- Taji I, Moayed MH, Mirjalili M (2015) Correlation between sensitization and pitting corrosion of AISI 403 martensitic stainless steel. *Corros Sci* 92:301–308. <https://doi.org/10.1016/j.corsci.2014.12.009>
- Park J-Y, Park Y-S (2006) Effects of austenitizing treatment on the corrosion resistance of 14Cr-3Mo martensitic stainless steel. *Corros* 62:541–547. <https://doi.org/10.5006/1.3279913>
- Vinas J, Brezinova J, Guzanova A, Svetlik J (2013) Degradation of renovation layers deposited on continuous steel casting rollers by submerged arc welding. *Proc Inst Mech Eng Part B J Eng Manuf* 227:1841–1848. <https://doi.org/10.1177/0954405413493405>
- Du Toit M, Van Niekerk J (2010) Improving the life of continuous casting rolls through submerged arc cladding with nitrogen-alloyed martensitic stainless steel. *Weld World* 54:R342–R349
- Zhang S, Wang P, Li D, Li Y (2015) Investigation of the evolution of retained austenite in Fe–13%Cr–4%Ni martensitic stainless steel during intercritical tempering. *Mater Des* 84:385–394. <https://doi.org/10.1016/j.matdes.2015.06.143>
- Da Silva GF, Tavares SSM, Pardal JM, Silva MR, De Abreu HFG (2011) Influence of heat treatments on toughness and sensitization of a Ti-alloyed supermartensitic stainless steel. *J Mater Sci* 46:7737–7744. <https://doi.org/10.1007/s10853-011-5753-8>
- Mokhtabad Amrei M, Yves A, Florent V, Denis B (2015) Microstructure characterization of single and multipass 13Cr4Ni steel welded joints. *Metallogr Microstruct Anal* 4:207–218. <https://doi.org/10.1007/s13632-015-0202-8>
- Divya M, Das CR, Mahadevan S, Albert SK, Pandian R, Kar SK, Bhaduri AK, Jayakumar T (2015) Influence of PWHT on toughness of high chromium and nickel containing martensitic stainless steel weld metals. *Metall Mater Trans A* 46:2554–2567. <https://doi.org/10.1007/s11661-015-2847-y>
- Akselsen OM, Rorvik G, Kvaale PE, Van Der Eijk C (2004) Microstructure-property relationships in HAZ of new 13% Cr martensitic stainless steels. *Weld J* 83:160-s–167-s
- Thibault D, Bocher P, Thomas M (2009) Residual stress and microstructure in welds of 13%Cr-4%Ni martensitic stainless steel. *J Mater Process Tech* 209:2195–2202. <https://doi.org/10.1016/j.jmatprotec.2008.05.005>
- Bilmes P, Llorente C, Pe J (2000) Toughness and microstructure of 13Cr4NiMo high-strength steel welds. *J Mater Eng Perform* 9:609–615. <https://doi.org/10.1361/105994900770345458>
- Tang YS, Juang SC, Chang CH (2002) The use of grey-based Taguchi methods to determine submerged arc welding process parameters in hardfacing. *J Mater Process Technol* 128:1–6. [https://doi.org/10.1016/S0924-0136\(01\)01261-4](https://doi.org/10.1016/S0924-0136(01)01261-4)
- Scotti A, Albuquerque Rosa LA (1997) Influence of oscillation parameters on crack formation in automatic Fe-B hardfacing. *J Mater Process Technol* 65:272–280. [https://doi.org/10.1016/S0924-0136\(96\)02415-6](https://doi.org/10.1016/S0924-0136(96)02415-6)
- Wang P, Lu SP, Xiao NM, Li DZ, Li YY (2010) Effect of delta ferrite on impact properties of low carbon 13Cr-4Ni martensitic stainless steel. *Mater Sci Eng A* 527:3210–3216. <https://doi.org/10.1016/j.msea.2010.01.085>
- Du Toit M, Van Rooyen GT, Smith D (2007) An overview of the heat-affected zone sensitization and stress corrosion cracking behaviour of 12% chromium type 1.4003 ferritic stainless steel. *Weld World* 51:41–50
- Barnhouse EJ, Lippold JC (1998) Microstructure/property relationships in dissimilar welds between duplex stainless steels and carbon steels. *Weld J* 77:477-s–487-s
- Gesnoui C, Hazarabedian A, Bruzzoni P, Ovejero-García J, Bilmes P, Llorente C (2004) Effect of post-weld heat treatment on the microstructure and hydrogen permeation of 13CrNiMo

- steels. *Corros Sci* 46:1633–1647. <https://doi.org/10.1016/j.corsci.2003.10.006>
18. Gesnoin C, Sharkawy SW, Dietzel W (2004) Hydrogen assisted stress-cracking behaviour of electron beam welded supermartensitic stainless steel weldments. *Mater Sci Eng A* 385:6–12. <https://doi.org/10.1016/j.msea.2004.03.029>
 19. Carrouge D, Bhadeshia HKDH, Woollin P (2004) Effect of δ - ferrite on impact properties of supermartensitic stainless steel heat affected zones. *Sci Technol Weld Join* 9:377–389. <https://doi.org/10.1179/136217104225021823>
 20. Balmforth M, Lippold JC (2000) A new ferritic-martensitic stainless steel constitution diagram. *Weld J* 79:33-s–345-s http://www.aws.org/w/a/wj/supplement/WJ_2000_12_s339.pdf
 21. Gooch TG (1977) Welding martensitic stainless steels. *Weld Inst Res Bull* 18:343–349
 22. Self JA, Olson DA, Edwards GR (1984) The stability of austenitic weld metal. *Proceedings of IMCC*, Kiev
 23. Folkhard E (1988) *Welding metallurgy of stainless steels*. Springer-Verlag, Wien
 24. ASM International (1991) *Metals handbook*, vol 4 Ohio
 25. Lippold JC, Kotecki DJ (2005) *Welding metallurgy and weldability of stainless steels*. Wiley, Hoboken
 26. Divya M, Das CR, Ramasubbu V, Albert SK, Bhaduri AK (2011) Improving 410NiMo weld metal toughness by PWHT. *J Mater Process Technol* 211:2032–2038. <https://doi.org/10.1016/j.jmatprotec.2011.06.024>
 27. Ladanova E, Solberg JK, Rogne T (2006) Carbide precipitation in HAZ of multipass welds in titanium containing and titanium free supermartensitic stainless steels Part 2 – Weld simulation studies. *Corros Eng Sci Technol* 41:152–160. <https://doi.org/10.1179/174327806X107923>
 28. Alonso-Falleiros N, Magri M, Falleiros IGS (1999) Intergranular corrosion in a martensitic stainless steel detected by electrochemical tests. *Corrosion* 55:769–778. <https://doi.org/10.5006/1.3284032>

Publisher's note Springer Nature remains neutral with regard to jurisdictional claims in published maps and institutional affiliations.